

Spitzer and Hubble Constraints on the Physical Properties of the $z \sim 7$ Galaxy Strongly Lensed by Abell 2218^{1,2}

E. Egami³, J.-P. Kneib^{4,5}, G. H. Rieke³, R. S. Ellis⁵, J. Richard^{4,5}, J. Rigby³, C. Papovich³, D. Stark⁵, M. R. Santos⁶, J.-S. Huang⁷, H. Dole³, E. Le Floc'h³, and P. G. Pérez-González³

ABSTRACT

We report the detection of a $z \sim 7$ galaxy strongly lensed by the massive galaxy cluster Abell 2218 ($z = 0.175$) at 3.6 and 4.5 μm using the *Spitzer Observatory* and at 1.1 μm using the *Hubble Space Telescope*. The new data indicate a refined photometric redshift in the range of 6.6 – 6.8 depending on the presence of Ly α emission. The spectral energy distribution is consistent with having a significant Balmer break, suggesting that the galaxy is in the poststarburst stage with an age of at least ~ 50 Myr and quite possibly a few hundred Myr. This suggests the possibility that a mature stellar population is already in place at such a high redshift. Compared with typical Lyman break galaxies at $z \sim 3 - 4$, the stellar mass is an order of magnitude smaller ($\sim 10^9 M_\odot$), but the specific star formation rate (star formation rate/ M_{star}) is similarly large ($> 10^{-9} \text{ yr}^{-1}$), indicating equally vigorous star-forming activity.

Subject headings: cosmology: observations — galaxies: formation — galaxies: evolution — galaxies: high-redshift — gravitational lensing

¹This work is based in part on observations made with the Spitzer Observatory, which is operated by the Jet Propulsion Laboratory, California Institute of Technology under NASA contract 1407. Support for this work was provided by NASA through Contract Number 960785 issued by JPL/Caltech.

²Based on observations made with the NASA/ESA Hubble Space Telescope, obtained at the Space Telescope Science Institute, which is operated by the Association of Universities for Research in Astronomy, Inc., under NASA contract NAS 5-26555. These observations are associated with program #9452.

³Steward Observatory, University of Arizona, 933 N. Cherry Avenue, Tucson, AZ85721

⁴Observatoire Midi-Pyrénées, UMR5572, 14 Avenue Edouard Belin, 31000 Toulouse, France

⁵Department of Astronomy, California Institute of Technology, 105-24, Pasadena, CA91125

⁶Institute of Astronomy, Madingley Road, Cambridge, CB3 0HA, UK

⁷Harvard-Smithsonian Center for Astrophysics, 60 Garden Street, Cambridge, MA02138

1. Introduction

Locating and characterizing the first sub-galactic sources which may have been responsible for completing cosmic reionization and ending the “Dark Ages” represents the latest frontier in observational cosmology. Although gravitational instability theory allows the early formation of massive halos (e.g., Barkana & Loeb 2000), the complexities of gas cooling, star formation, feedback and the clumpiness of the intergalactic medium make observational predictions highly uncertain (Stiavelli, Fall, & Panagia 2004). Data on representative early sources are needed to better understand when reionization occurred as well as what the luminosity and mass functions are of the sources responsible for the reionization.

Searching for representative sources at redshift (z) of 6–10, the range considered to be the final stages of the reionization era, is a major observational challenge, not only because of the large luminosity distances involved but also since (as predicted by the hierarchical model of galaxy formation) the most likely systems to be found during this period have lower stellar masses than those at more moderate redshifts. The high magnification associated with strong gravitational lensing by massive foreground clusters offers a unique opportunity for detecting such galaxies. In recent years, this approach has been employed specifically to find galaxies during the reionization era, and has produced a number of successes (Ellis et al. 2001; Hu et al. 2002; Santos et al. 2004; Kneib et al. 2004a). The detection of a $z \sim 10$ galaxy by Pelló et al. (2004), however, is controversial (Weatherley et al. 2004; Bremer et al. 2004).

In this Letter, we return to analyze in more detail the physical characteristics of the triply lensed $z \sim 7$ source in Abell 2218 ($z = 0.175$) reported by Kneib et al. (2004a). The original redshift estimate was based on three pieces of observational evidence obtained for the two brighter components a (RA: 16:35:54.73, DEC: 66:12:39.0; J2000) and b (RA: 16:35:54.40, DEC: +66:12:32.8; J2000): (1) reflection symmetry with respect to the well-defined $z \gtrsim 6$ critical lines, (2) photometric redshift suggesting $6.6 < z < 7.1$, and (3) a tentative spectroscopic detection of a continuum break at 9800 Å, which, if due to Gunn-Peterson absorption at Ly α , would indicate $z = 7.05$. Here, we report the *Spitzer* detection at 3.6 and 4.5 μm of these two components as well as the new 1.1 μm detection by the *Hubble Space Telescope* (*HST*). With these new data, we will refine the photometric redshift and examine the physical properties of this lensed galaxy.

2. Observations

The 3.6 and 4.5 μm images were obtained on UT 2004 January 2 with the InfraRed Array Camera (IRAC; Fazio et al. (2004)) on the *Spitzer Observatory*. In each filter, twelve 200-second images were taken with the small-step cycling dither pattern. The Basic Calibrated Data (BCD) images were combined using a custom IDL mosaicking routine with the final pixel scale of $0''.6 \text{ pixel}^{-1}$, half of the instrument pixel size. The IRAC observations also provided 5.8 and 8.0 μm images of the same field simultaneously, but the $z \sim 7$ galaxy was not detected at these longer wavelengths.

The 1.1 μm images were obtained on UT 2004 March 23 with the Near Infrared Camera and Multi-Object Spectrometer (NICMOS) on *HST*. A total of nine 2304 second (using the SPARS256 sequence) and one 1472 second (using the SPARS64 sequence) exposures were taken with the F110W filter using the NIC3 camera, which has a pixel scale of $0''.2 \text{ pixel}^{-1}$.

The central wavelengths and full widths at 20% of the transmission peak are listed in Table 1 for all the observed bands based on the total transmission curves.

3. Results

Figure 1 shows the *HST*/NICMOS and *Spitzer*/IRAC images. Components *a* and *b* of the galaxy reported by Kneib et al. (2004a) are clearly detected at 1.1 μm (Figure 1a). At 3.6 and 4.5 μm , component *b* is clearly detected while component *a* is seen as a faint extension to the northwest of the $z = 2.5$ lensed submillimeter source SMM-A (SMM J16359+6612.6) discussed by Kneib et al. (2004b) (Figure 1b and c). For comparison, the *HST*/NICMOS 1.6 μm image by Kneib et al. (2004a) is also displayed (Figure 1d), which shows the two components and SMM-A with a higher signal-to-noise ratio. When the light from SMM-A is subtracted using a two-dimensional elliptical Gaussian, component *a* shows up in the IRAC images (Figures 1e and f).

At 1.1 μm , photometry was performed in a manner consistent with that in Kneib et al. (2004a), giving the total fluxes of components *a* and *b*. In the IRAC bands, photometry was performed only for component *b* because the flux measurements with component *a* are highly uncertain due to the subtraction of SMM-A. For the photometry of component *b*, we used an elliptical aperture with semi-major and semi-minor axes of $2''$ and $1''$, respectively, and aligned the major axis along the position angle of component *b* (23 degrees East of North). Because of the large point spread functions at 3.6 and 4.5 μm (FWHM $\sim 1''.7$), the elliptical aperture misses a significant fraction of the total source flux. By convolving the F160W image with the IRAC PSFs, we determined that the flux measured with the

elliptical aperture needs to be multiplied by a factor of 1.4 to account for this missing flux (i.e., aperture correction).

The sky level was measured using similar ellipses to define the inner and outer boundaries of a sky area with a semi-major axis of 2 and 3.5 pixels, respectively. There is a slight sky background gradient along the east-west direction due to the bright source to the west, but the component *b* is far enough from this source that the gradient is quite linear across component *b* and the surrounding sky area. Therefore, we expect this gradient to be removed if we derive the local sky level as the average of all the sky pixel values. We also visually inspected the image cross sections, and confirmed that the derived sky level is a good estimate around the position of component *b*. The photometric uncertainty is based on the scatter of sky pixel values, and our estimates are conservative in that the scatter not only includes the random sky pixel noise but is also inflated by the sky gradient along the east-west direction.

The measured flux densities at 1.1, 3.6, and 4.5 μm are listed in Table 1 together with the previous *HST* measurements presented in Kneib et al. (2004a). The 1.1 and 1.6 μm images show a faint source north-west of component *b*. This source is also seen in the F606W, F814W, and F850LP images (Kneib et al. 2004a). The *Spitzer* images provide enough spatial resolution to conclude that there is very little flux emitted by this bluer and less distant source at 3.6 and 4.5 μm .

4. Discussion

The new photometric data permit us to construct the spectral energy distribution (SED) of component *b*, which we compare with the model SEDs simulated using the stellar population synthesis code GALAXEV (Bruzual & Charlot 2003). A grid of models was calculated with the parameters described in Table 2. The intrinsic (i.e., unmagnified) flux densities were assumed to be 25 times smaller than the observed values (Kneib et al. 2004a). For each model, the best-fit SED was sought by varying age and redshift and minimizing χ^2 . The predicted fluxes were calculated from the model SEDs with appropriate total system throughput curves. The overall normalization of a model SED was determined by the F160W flux density measurement, which has the highest signal-to-noise ratio. This leaves five filters (F814W, F850LP, F110W, IRAC 3.6 and 4.6 μm) to constrain the SED shape.

Given that little is known about the mode of star formation at $z > 6$, we tried to bracket various parameter ranges by calculating models for four different star formation histories: exponentially decaying burst models with the star formation rate (SFR) e-folding times (τ) of 10, 50, 100 Myrs as well as the 1 Gyr burst (constant SFR) model. These models

should encompass realistic star formation time scales. An instantaneous burst model, though unphysical, was also included for comparison. The GALAXEV results were cross-checked against Starburst99 (Leitherer et al. 1999), which gave similar results.

Figure 2a shows the best (i.e., minimum χ^2) SEDs for each star formation history. The corresponding model parameters are listed in Table 2. All the model fits consistently give a redshift of 6.60–6.65. If we model the SED including Ly α emission line with an observed equivalent width of 100–300 Å, the photometric redshift could increase up to $z \simeq 6.8$. (This addition of a Ly α line changes redshift, but does not affect the physical properties of the stellar population significantly.) The existence of such a Ly α line is still consistent with the spectra presented by Kneib et al. (2004a) since there are a number of strong atmospheric OH lines in their wavelength range. A redshift above 6.8, however, is unlikely because it would require strong Ly α emission, which would have been seen in the near-infrared spectrum in Kneib et al. (2004a). This suggests that the continuum break at 9800 Å seen by Kneib et al. (2004a) is either spurious or an absorption line feature.

Figure 2 also illustrates the importance of having *Spitzer*/IRAC photometry for such a high redshift galaxy. IRAC measures the SED above 4000 Å in the restframe, thereby constraining the strength of the Balmer break. The IRAC measurements are indicative of a significant Balmer break (Figure 2), suggesting that the galaxy is observed well after the most vigorous stage of star formation (i.e., poststarburst), which is consistent with the fact that all the exponentially decaying SFR models consistently give a galaxy age larger than the SFR e-folding time. A precise determination of the galaxy age, however, is difficult because it essentially depends on the star formation history we assume (Table 2). A reasonable lower limit on the age seems to be $\sim 50 - 60$ Myr based on the $\tau = 10$ Myr model (ignoring the instantaneous model, which is informative but unrealistic). The upper limit, on the other hand, is harder to constrain, and the 1 Gyr burst model is consistent with an age range of 300–700 Myrs (68% confidence interval), the large uncertainty being due to the slow SED evolution of this model in this age range. Taken as a whole, the model calculations in Table 2 suggest the existence of a mature stellar population whose age is at least 50 Myr and quite possibly a few hundred Myr.

An interesting characteristic inferred from the model fits is an extremely blue restframe UV spectrum. The spectral slope index β (defined as $f_\lambda \propto \lambda^\beta$) is $\lesssim -2$, as is the case with the lower redshift UDF *i*-dropout galaxies for which NICMOS photometry is available (Stanway et al. 2004). Such a UV spectrum is consistent with a recent starburst and a normal IMF, but requires low extinction and/or low metallicity. Unfortunately, extinction and metallicity are degenerate, and are difficult to constrain independently with our photometric resolution. As an example, we show this degeneracy for the case of the $\tau = 100$ Myr model in Figure 2b

(Table 2 lists the corresponding model parameters).

By including the full range of models that produce acceptable fits in addition to those listed in Table 2, the various galaxy parameters are constrained to the following ranges (instantaneous models excluded): redshift: 6.6–6.8; age: 50–450 Myr; stellar mass: $0.5–1 \times 10^9 M_\odot$; and SFR: $0.1–5 M_\odot \text{ yr}^{-1}$. These numbers reflect the ranges of the best-fit parameters without including the parameter uncertainties associated with each fit. As already discussed, it is not possible to constrain the age accurately without knowing the actual star formation history. The mass is better constrained than the age, and the estimated mass ($\sim 10^9 M_\odot$) is an order of magnitude smaller than those of typical Lyman break galaxies at $z = 3 – 4$ ($\sim 10^{10} M_\odot$) (Papovich, Dickinson, & Ferguson 2001; Shapley et al. 2001; Barmby et al. 2004). However, the specific star formation rate ($\text{SFR}/M_{\text{star}}$) (e.g., Brinchmann et al. 2004) is similarly large ($> 10^9 \text{ yr}^{-1}$), indicating equally vigorous star-forming activity.

The possible detection of a mature stellar population in this galaxy allows us to extend the argument made by Kneib et al. (2004a) on the basis of the high surface density on the sky of sources similar to that studied here. As implied by its discovery in a small survey area, unless we have been extraordinarily fortunate, such sources are likely to have a mean surface density of $\simeq 1 \text{ arcmin}^{-2}$ and remain luminous over an extend period of cosmic history. Accordingly, it is likely that they contribute significantly to the UV photon budget necessary for cosmic reionization.

5. Conclusions

The new *Spitzer* and *HST* data indicate that the redshift of this lensed galaxy is indeed very high, probably at $z \sim 6.6 – 6.8$. Comparison with a variety of stellar population synthesis models indicates that the galaxy is in the poststarburst stage with an age of at least ~ 50 Myr and quite possibly a few hundred Myr, which suggests the possibility that a mature stellar population is already in place at such a high redshift. Unless we have been fortunate in its discovery, it is likely that such sources with extended lifetimes contribute significantly to cosmic reionization.

We acknowledge helpful discussions with G. Smith, D. Stern, R. Pello, D. Schaefer, and thank G. Neugebauer for commenting on the manuscript. JPK acknowledges support from Caltech and CNRS. The study of Abell 2218 as a cosmic lens is supported by NASA STScI grant HST-GO-09452.01-A.

REFERENCES

Barkana, R. & Loeb, A. 2000, *ApJ*, 531, 613

Barmby, P., et al. 2004, *ApJS*, in press (astro-ph/0405624)

Bremer, M. N., Jensen, J. B., Lehnert, M.D., Förster-Schreiber, N. M., & Douglas, L. 2004, *ApJ*, in press (astro-ph/0409485)

Brinchmann, J., Charlot, S., White, S. D. M., Tremonti, C., Kauffmann, G., Heckman, T., & Brinkmann, J. 2004, *MNRAS*, 351, 1151

Bruzual, G., & Charlot, S. 2004, *MNRAS*, 344, 1000

Charlot, S., & Fall, S. M. 2000, *ApJ*, 539, 718

Ellis, R., Santos, M. R., Kneib, J., & Kuijken, K. 2001, *ApJ*, 560, L119

Fazio, G. G., et al. 2004, *ApJS*, in press (astro-ph/0405616)

Hu, E. M., Cowie, L. L., McMahon, R. G., Capak, P., Iwamuro, F., Kneib, J.-P., Maihara, T., & Motohara, K. 2002, *ApJ*, 568, L75

Kneib, J., Ellis, R. S., Santos, M. R., & Richard, J. 2004a, *ApJ*, 607, 697

Kneib, J., van der Werf, P. P., Kraiberg Knudsen, K., Smail, I., Blain, A., Frayer, D., Barnard, V., & Ivison, R. 2004b, *MNRAS*, 349, 1211

Leitherer, C., et al. 1999, *ApJS*, 123, 3

Papovich, C., Dickinson, M., & Ferguson, H. C. 2001, *ApJ*, 559, 620

Pelló, R., Schaerer, D., Richard, J., Le Borgne, J.-F., & Kneib, J.-P. 2004, *A&A*, 416, L35

Santos, M. R., Ellis, R. S., Kneib, J., Richard, J., & Kuijken, K. 2004, *ApJ*, 606, 683

Shapley, A. E., Steidel, C. C., Adelberger, K. L., Dickinson, M., Giavalisco, M., & Pettini, M. 2001, *ApJ*, 562, 95

Stanway, E. R., McMahon, R. G., & Bunker, A.J. 2004, *MNRAS*, submitted (astro-ph/0403585)

Stiavelli, M., Fall, S. M., & Panagia, N. 2004, *ApJ*, 600, 508

Weatherley, S. J., Warren, S. J., & Babbedge, T. S. R. 2004, *MNRAS*, submitted (astro-ph/0407150)

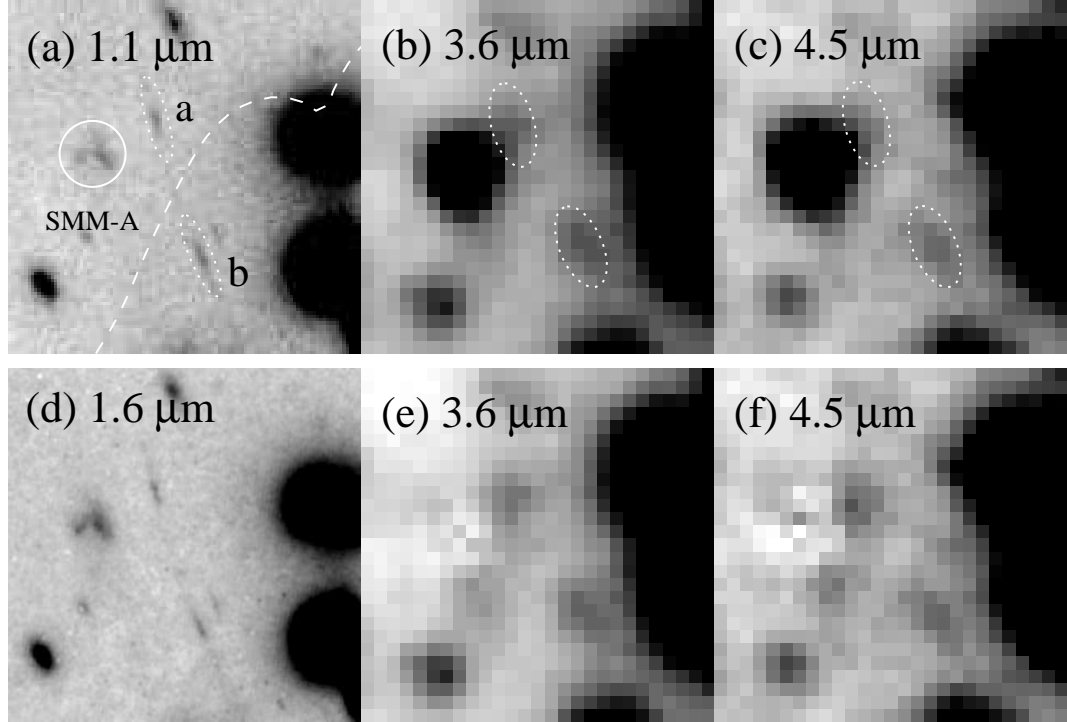


Fig. 1.— *HST*/NICMOS and *Spitzer*/IRAC images of the $z \sim 7$ lensed pair: (a) New NICMOS 1.1 μm image. Components a and b as well as the $z=2.5$ submillimeter source SMM-A are marked. The dashed line indicates the $z \gtrsim 6.5$ critical curves; (b) IRAC 3.6 μm image; (c) IRAC 4.5 μm image; (d) NICMOS 1.6 μm image presented in Kneib et al. (2004a); (e) IRAC 3.6 μm image with SMM-A subtracted; (f) IRAC 4.5 μm image with SMM-A subtracted. Each image is 16'' on a side. In the panels (a) and (d), north is up and east is to the left. In the panels (b), (c), (e), and (f), we preserved the original array orientation, which is 11° rotated counter-clockwise from that of the panels (a) and (b), in order to display the results of the SMM-A subtraction accurately. The dashed-line ellipses shown in (b) and (c) around component b indicate the areas used for photometry. Similar ellipses are drawn around component a to mark its position.

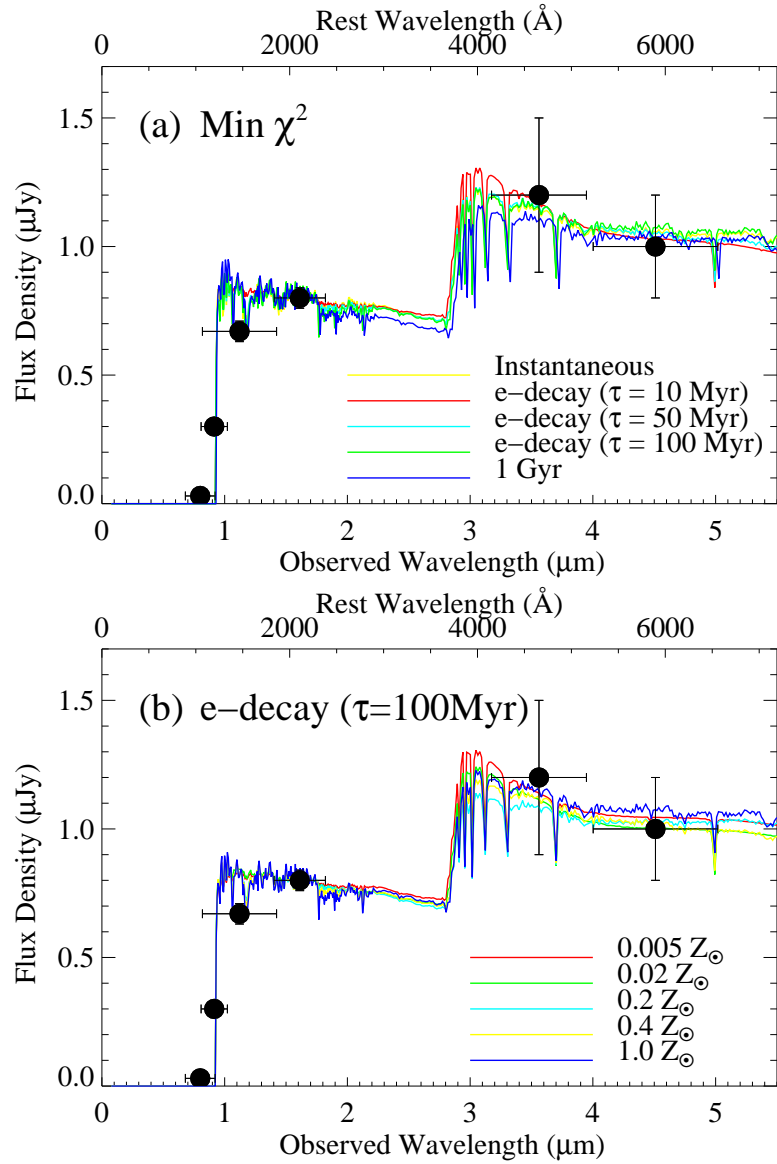


Fig. 2.— SED model fits to the observed SED of the $z \sim 7$ galaxy (component *b*): (a) The best (i.e., minimum χ^2) model for each star formation history; (b) the exponentially decaying starburst model ($\tau = 100$ Myr) for a range of metallicities. The restframe wavelength at $z = 6.65$ is also shown. The error bars indicate the $\Delta\lambda$ and flux density uncertainty of each band shown in Table 1. The measured flux at $1.1 \mu\text{m}$ is expected to be significantly lower than the true continuum level because the F110W filter passband extends below 1216\AA in the restframe.

Table 1. Flux densities of components *a* and *b*

Filter	λ_c ^a (μm)	$\Delta\lambda$ (20%) ^a (μm)	Flux density	
			a (μJy)	b (μJy)
<i>F814W</i>	0.801	0.242	0.09±0.02	0.03±0.01
<i>F850LP</i>	0.915	0.214	0.39±0.02	0.30±0.02
<i>F110W</i>	1.121	0.604	0.78±0.05	0.67±0.04
<i>F160W</i>	1.612	0.418	0.87±0.04	0.80±0.04
3.6 μm	3.561	0.773	...	1.2±0.3
4.5 μm	4.510	1.015	...	1.0±0.2

^aThe effective wavelength and the full width at 20% of the peak calculated from the total transmission curves.

Note. — The IRAC flux densities of component *a* are highly uncertain due to the subtraction of SMM-A, and therefore are not listed.

Table 2. Model parameters

Model	Metallicity (Z_{\odot})	z	Age ^a (Myr)	Mass ($10^8 M_{\odot}$)	τ_V	SFR (M_{\odot}/yr)	z_{form}
Minimum χ^2 models							
Instantaneous burst	0.4	6.60	35 (28-40)	5.5	0.25	...	6.8
e-decaying burst ($\tau = 10$ Myr)	0.02	6.60	64 (56-72)	8.2	0.50	0.2	7.0
e-decaying burst ($\tau = 50$ Myr)	0.4	6.60	102 (82-114)	6.3	0.25	2.2	7.3
e-decaying burst ($\tau = 100$ Myr)	1.0	6.65	181 (150-201)	8.3	0.0	2.0	8.1
1 Gyr burst	1.0	6.65	453 (287-693)	9.7	0.0	2.6	12.3
e-decaying ($\tau = 100$ Myr) models with sub-solar metallicities							
e-decaying burst ($\tau = 100$ Myr)	0.005	6.60	161 (121-185)	11	0.75	3.3	7.8
	0.02	6.60	143 (124-175)	8.5	0.50	3.2	7.7
	0.2	6.60	90 (66-120)	5.4	0.50	4.2	7.2
	0.4	6.60	128 (105-156)	6.2	0.25	2.8	7.5

^aThe numbers in parentheses indicate the 68% confidence interval based on $\Delta\chi^2$.

Note. — Models with GALAXEV (Bruzual & Charlot 2003) explored the following range of parameters: (1) Initial mass function (IMF): Salpeter with the lower and upper mass cutoffs of 0.1 and 100 M_{\odot} ; (2) metallicity: 0.005, 0.02, 0.2, 0.4, 1.0, and 2.5 Z_{\odot} ; (3) dust extinction: $\tau_V = 0.0, 0.25, 0.5, 0.75, 1.0, 1.25$, and 1.5, where τ_V is the total effective V -band optical depth seen by young (age $< 10^7$ yrs) stars. The optical depth toward old stars (age $> 10^7$ yrs) was set to be 1/3 of this. See Charlot & Fall (2000) and Bruzual & Charlot (2003) for more detail; and (4) star formation histories: instantaneous burst, exponentially decaying burst ($\text{SFR} \propto e^{-t/\tau}$, where t is the galaxy age and τ is the SFR e-folding time scale) with $\tau = 10, 50$, and 100 Myr, and 1 Gyr burst (a constant SFR model with the SFR scaled such that all the gas gets consumed in 1 Gyr). The flux below Ly α ($\lambda_{rest} = 1216$ Å) was set to zero, and no Ly α emission line was included. SFRs listed are intrinsic model values. We assumed a magnification factor of 25 (Kneib et al. 2004a) and the cosmological parameters of $\Omega_M = 0.3$, $\Omega_{\Lambda} = 0.7$ and $H_0 = 70$ km s^{-1} Mpc^{-1} .